ASME Letters in Dynamic Systems and Control. Received August 20, 2020;
Accepted manuscript posted April 01, 2021. doi:10.1115/1.4050957

TOWARDS A MOBILE ROBOT FOR VIBRATION CONTROL AND INSPECTION OF POWER LINES

Paul-Camille Kakou
Vibrations and Robotics Laboratory
Department of Mechanical Engineering
Virginia Polytechnic and State University
Blacksburg, Virginia 24061
Email: paulc97@vt.edu

Oumar Barry*
Vibrations and Robotics Laboratory
Department of Mechanical Engineering
Virginia Polytechnic and State University
Blacksburg, Virginia 24061
Email: obarry@vt.edu

ABSTRACT

As power demand across communities increases, focus has been given to the maintenance of power lines against harsh environments such as wind-induced vibration (WIV). Inspection robots and fixed vibration absorbers (FVAs) are the current solutions. However, both solutions are currently facing many challenges. Inspection robots are limited by their size and considerable power demand, while FVAs are narrowband and unable to adapt to changing wind characteristics, and thus are unable to reposition themselves at the antinodes of the vibrating loop. In view of these shortcomings, we propose a mobile damping robot (MDR) that integrates inspection robots mobility and FVAs WIV vibration control to help maintain power lines. In this effort, we model the conductor and the MDR by using Hamilton's principle and we consider the two-way nonlinear interaction between the MDR and the cable. The MDR is driven by a Proportional-Derivative (PD) controller to the optimal vibration location (antinodes) as the wind characteristics vary. The numerical simulations suggest that the MDR outperforms FVAs for vibration mitigation. Furthermore, the key parameters that influence the performance of the MDR are identified through a parametric study. The findings could set up a platform to design a prototype and experimentally evaluate the performance of the MDR.

INTRODUCTION

Wind-induced vibration (WIV) is a major concern for flexible engineering structures such as airplane wings, spacecraft, power transmission lines, and cable-stayed bridge (see Fig.1). For power transmission lines, these oscillatory motions typically take the form of Aeolian vibrations, which are caused by vortex shedding and are relatively high-frequency, low-amplitude vibrations. Aeolian vibration frequencies vary between 3 and 150 Hz, and the peak-to-peak amplitude is usually smaller than the cable diameter [1–7].

*Address all correspondence to this author.

ASME Letters in Dynamic Systems and Control. Received August 20, 2020;
Accepted manuscript posted April 01, 2021. doi:10.1115/1.4050957

When left uncontrolled, WIV may lead to power lines (PLs) failure, thereby undermining public safety and resulting in considerable economic losses. The Department of Energy (DOE) reported that weather-related annual outage costs were estimated to be between $18 and $33 billion [8]. These unfortunate events have also resulted in deaths. The conventional methodology for vibration mitigation employs fixed passive vibration absorbers (FPVAs) (Fig. 1.a)). The problem with the FPVAs is that their effectiveness is dependent on the wind characteristics, which change with time, thus frequency and optimum absorber location (i.e. antinode of the vibrating loop) are also time-varying. These challenges can be overcome using a mobile damping robot (MDR) capable of adapting to the changing environment and move to an antinode.

Currently, the most common methods of power line inspection and maintenance are foot patrol, and helicopter-assisted inspection [9]. Both techniques are expensive, laborious, and can be dangerous for electrical technicians and pilots. For these reasons, numerous grid owners, institutions, and researchers have developed inspection robots [10–17]. However, the implementation of these inspection robots is limited by the cost, the high power demand, the short operation time, and the considerable weight. For instance, the LineScout robot developed by Hydro Quebec weighs about 120 kg [18] (Fig. 1-(b)) and the TI robot from EPRI is about 2 meters long [14]. We plan to transform our recent patent on passive WIV control to a robot for not only smart vibration control, but also for intelligent power line monitoring, inspection, and repair. Unlike conventional inspection robots, our novel robot will be lightweight, compact, and permanently mounted on the power lines.

To realize a MDR for intelligent WIV control and maintenance of power lines, we need to understand the linear abd nonlinear dynamic interactions of a moving robot, cable, and wind forces. Few researchers have explored the possibility of a moving damper for improved vibration suppression in manufacturing [19] and for civil structures [20, 21]. More recently Bukhari et al. [22] extended the moving vibration absorber idea to power lines. In that work, the mobile damper responded to a predefined profile of wind characteristics. However, it did not include an active controller to travel to the antinode as needed. In this study, we redefine the moving damper as an intelligent mobile damping robot and explore further its ability to suppress vibrations of PLs and carry out other tasks such as monitoring and inspection of PLs. To do so, we model the MDR with a proportional derivative controller to travel across the conductor using Hamilton's principle [23]. Then we provide a numerical analysis of the system carried out in MATLAB®. Finally, we perform a parametric study to determine the key parameters of the robot.

SYSTEM DESCRIPTION

This section presents the mathematical derivation of the mobile damping robot attached to a conductor as portrayed in Fig. 2. This concept was developed by integrating our recently patented Aeolian vibration damper [24] with an inspection robot. The conductor, the in-span mass, and the vibration damper [24] were reduced to an equivalent tensile Euler-Bernoulli beam with an in-span mass-spring-mass and viscous damping system (see Fig. 3). The combination of the in-span mass and suspended mass constitutes the total mass of the MDR. Note that modeling a conductor as a beam instead of a string is more accurate since it helps capture the flexural rigidity of the conductor [25].

Starting from the position vector of the beam, the in-span mass and the suspended absorber and using

ASME Letters in Dynamic Systems and Control. Received August 20, 2020;
Accepted manuscript posted April 01, 2021. doi:10.1115/1.4050957

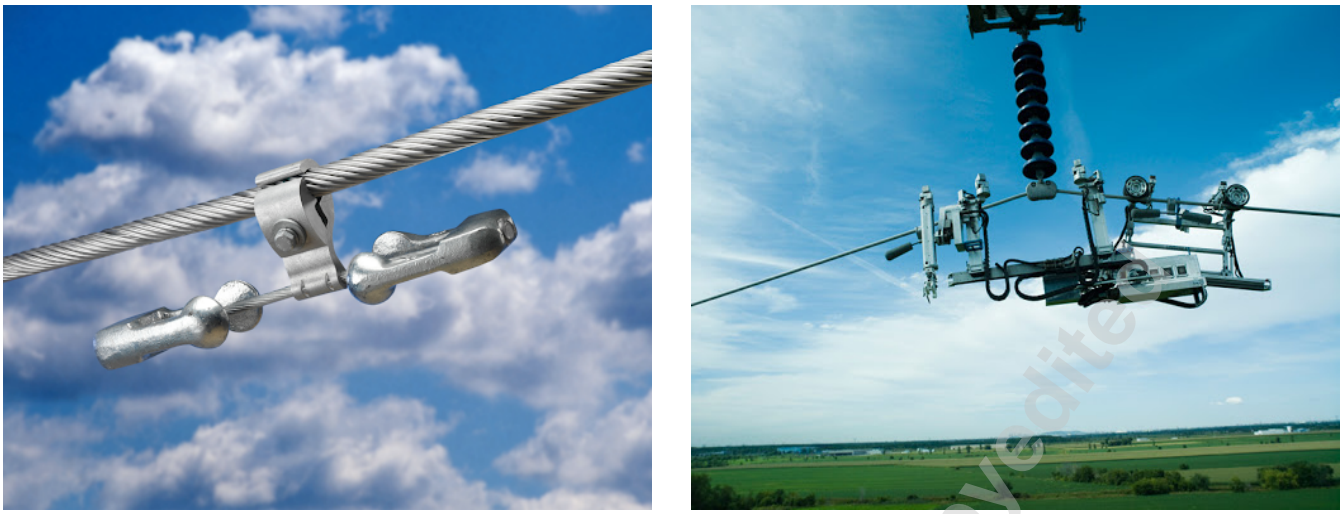

(a) Stockbridge Damper (b) Hydro-Quebec LineScout Inspection Robot

FIGURE 1: PRESENTATION OF A FIXED TVA AND AN INSPECTION ROBOT

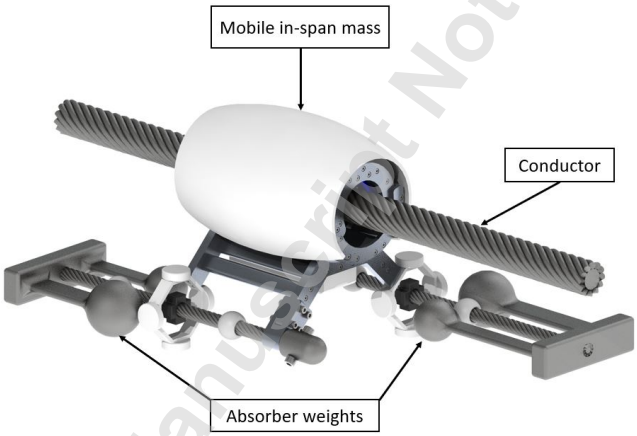

FIGURE 2: CONCEPTUAL DESIGN OF THE MOBILE DAMPING ROBOT ATTACHED TO A CONDUCTOR

Hamilton's principle, the governing equations of motion of the system can be expressed as

$$EIy^{''''} + m\ddot{y} + Ty^{''} = F(x,t) - (F_1 + F_2)\delta(x - x_c) \tag{1}$$

$$\Big[(m_a + m_c)\ddot{x}_c + m_c(\ddot{y} + 2\dot{y}^{'}v_a + y^{''}v_a^2 + y^{'}\ddot{x}_c)y^{'}\Big]\delta(x - x_c) = F_c \tag{2}$$

ASME Letters in Dynamic Systems and Control. Received August 20, 2020;
Accepted manuscript posted April 01, 2021. doi:10.1115/1.4050957

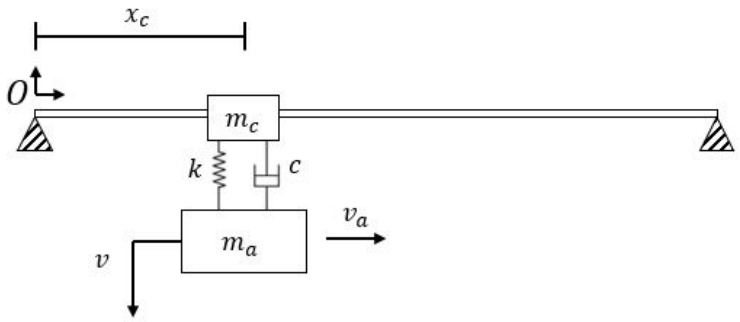

FIGURE 3: SCHEMATIC OF THE MOBILE DAMPING ROBOT ON THE CABLE

$$\left[m_a\ddot{v} - F_2\right]\delta(x - x_c) = 0 \tag{3}$$

The transverse displacement of the cable and the absorber are denoted by y and v, respectively. The longitudinal displacement and velocity of the MDR are denoted by x_c and v_a, respectively. EI is the flexural rigidity, m is the mass of the beam, T is the tension of the beam, m_c is the mass of the in-span mass, and m_a is the mass of the absorber. $\delta(x - x_c)$ represents the Dirac delta function used to determine the instantaneous location of the MDR. $F(x,t)$ is the uniform wind input force expressed as

$$F(t) = f_0 sin(\omega_n t) \tag{4}$$

where f_0 is the drag force defined as [22]:

$$f_0 = 0.5\rho D C_d V_w^2 \tag{5}$$

where D is the diameter of conductor, ρ is the density of fluid (wind), C_d is the drag coefficient, and V_w is the velocity of wind.

F_1, F_2 and F_c are given as

$$F_1 = m_c\left(\ddot{x}_c + \left(\ddot{y} + 2\dot{y}'\dot{x}_c + y''\dot{x}_c^2 + y'\ddot{x}_c\right)\right) \tag{6}$$

$$F_2 = k(y - v) + c\left(\dot{y} + y'\dot{x}_c - \dot{v}\right) \tag{7}$$

$$F_c = k_p(r - x_c) + k_d(\dot{r} - v_a) \tag{8}$$

In Equation 7, k represents the spring constant of the MDR and c represents its damping coefficient. In Equation 8, k_p and k_d represent the proportional and the derivative gain respectively. r represents the

position target while $\dot{r}$ represents the velocity target. In our model the position target can be determined based on the input wind force. For instance, if the wind input excites the first mode, the antinode will be located at the mid-span. It should be noted that this equation includes the nonlinear coupling forces i.e, centrifugal and Coriolis terms.

The vertical displacement of the cable is the solution to the EOMs. It can be expressed using the Galerkin decomposition method as

$$y(x,t) = \sum_{r=1}^{\infty} \Phi_r(x) A_r(t) \tag{9}$$

where $A_r(t)$ are time functions of the transverse displacement and $\Phi_r(x)$ are the normalized eigenfunctions (mode shapes). Following Barry et al. [4], the eigenfunctions are chosen as the mode shapes of a simply supported beam with tension as

$$\Phi_r(x) = \sqrt{\frac{2}{ml}} sin\left(\left(\sqrt{\frac{-T}{2EI} + \sqrt{\frac{T^2}{4(EI)^2} + \frac{m\omega_r^2}{EI}}}\right)x\right) \tag{10}$$

where the natural frequencies of the bare beam are given by

$$\omega_r = \left(\frac{\pi}{L}\right)\sqrt{\frac{EI}{m}\left(r^4 + \frac{r^2 T L^2}{\pi^2 EI}\right)} \tag{11}$$

Following [23, 26], Equations 1,2,3, which are a set of PDEs, can be transformed into ODEs for computation using the orthogonality condition. Assuming a constant MDR velocity, we obtain the following set of ODEs

$$\ddot{A}_p(t) + M_c\left[\sum_{r=1}^{\infty} \ddot{A}_r(t)\Phi_r(d) - 2\dot{A}_r(t)\Phi_r^{'}(d)v_a + A_r(t)\Phi_r^{''}(d)v_a^2\right]D_p(t) + 2\zeta\omega_p\dot{A}_p(t) + \omega_p^2 A_p(t)$$
$$+ \{k\left[\sum_{r=1}^{\infty} A_r(t)\Phi_r(d) - v(t)\right] + c\left[\sum_{r=1}^{\infty} A_r(t)\Phi_r(d) + A_r(t)\Phi_r^{'}(d)v_a - \dot{v}(t)\right]\}D_p(t) = N_p(t) \tag{12}$$

$$(M_a + M_c)\dot{v}_a(t) + M_c\left[\sum_{r=1}^{\infty} \ddot{A}_r(t)\Phi_r(d) - 2\dot{A}_r(t)\Phi_r^{'}(d)v_a + A_r(t)\Phi_r^{''}(d)v_a^2\right]A_r(t)\Phi_r^{'}(d)D_p(t) = k_p\Big(r - x_c(t)\Big) + k_d\Big(\dot{r} - \dot{x}_c(t)\Big) \tag{13}$$

ASME Letters in Dynamic Systems and Control. Received August 20, 2020;
Accepted manuscript posted April 01, 2021. doi:10.1115/1.4050957

$$M_a\ddot{v}(t) - k\left[\sum_{r=1}^{\infty} A_r(t)\Phi_r(d) - v(t)\right] + c\left[\sum_{r=1}^{\infty} A_r(t)\Phi_r(d) + A_r(t)\Phi_r^{'}(d)v_a - \dot{v}(t)\right] = 0 \tag{14}$$

where $N_p(t)$ and $D_p(t)$ can be defined as

$$N_p(t) = \int_0^L \Phi_r(x)F(x,t)dx, \quad r = 1, 2... \tag{15}$$

$$D_p(t) = \int_0^L \Phi_r(x)G(x,t)dx, \quad r = 1, 2... \tag{16}$$

and d is the position of absorber, which is equal to $v_a t$.

It is important to note that unlike in [22] in which a step function was employed to sequentially move the robot, here we determine the location of the antinode and select values for k_p and k_d to effectively drive the absorber to a desired position.

Numerical Simulations

The numerical simulations were performed on a 200-meter span length, using 795 Drake ACSR cable. The cable as well as the uniformly distributed load parameters are presented in Table 1. The cable natural frequencies were determined and used as wind excitation inputs. Table 2 lists five different cable modes. We note that the fundamental frequency falls outside of the Aeolian vibration frequency range (3Hz-150Hz). The other frequencies presented in the table corresponds to frequencies within the Aeolian vibration frequency range.

TABLE 1: PARAMETERS OF THE CABLE AND APPLIED LOAD

L(m)	m(kg/m)	T(N)	$EI(N.m^2)$	w_n(rad/s)	f_0(N/m)
200	1.6286	27840	1602	w_n	Eq. 5

Next, we verify that regardless of the simulation method, we can obtain the same results. Hence, we simulate the model of the MDR attached to the conductor using two MATLAB computation methods. The two methods considered are Bode and ODE45. Each computation method relies on distinct theories. The Bode function is used by defining the transfer function of the system and by analyzing the frequency response. The ODE45 method is founded on the acceleration analysis of the system using the EOMs. As shown in Figure 4, both methods generate the same results. This particular experiment can be extended to determine the optimal placement of the robot as we will discuss in the subsequent sections.

ASME Letters in Dynamic Systems and Control. Received August 20, 2020;
Accepted manuscript posted April 01, 2021. doi:10.1115/1.4050957

TABLE 2: PARAMETERS OF THE MOBILE ROBOT

m_c(m)	m_a(kg/m) (N)	$k(N/m)$	$c(Ns/m)$	k_p	k_d
24.8	1.30	$m_a * \omega_n^2$	5	1	6

TABLE 3: FIRST FIVE NATURAL FREQUENCIES FOR A 200 METER CABLE IN Hz

w_1	w_{10}	w_{16}	w_{30}	w_{60}
0.32	3.27	5.23	9.87	20.11

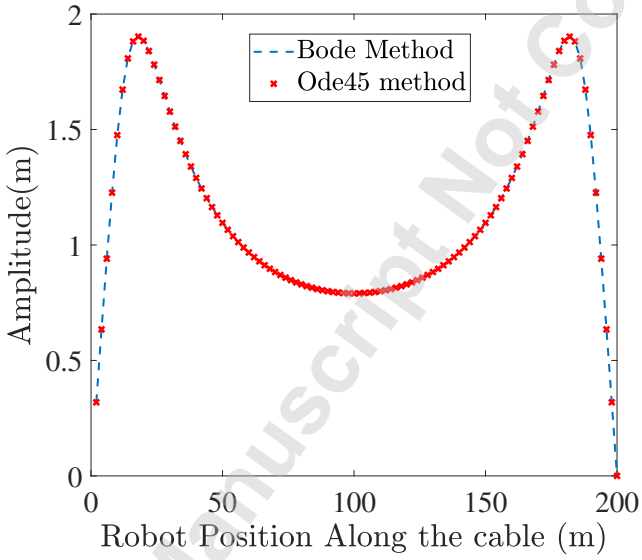

FIGURE 4: MODEL VALIDATION BY COMPARING THE RESPONSE OF THE CABLE-ROBOT SYSTEM USING TWO METHODS: ODE45 AND BODE. THE CABLE IS EXCITED BY A UNIFORMLY DISTRIBUTED WIND FORCE

Having validated the mathematical model, we provide a presentation of the PD controller used for the proposed MDR. The robot relies on a control scheme to move to the antinode and help mitigate the vibration of the cable. To determine the proportional and derivative gains for optimal control, the control requirements for the design need to be specified. The mobile robot is also required to reach the antinode in a reasonable amount of time and hence the rise time is also a key design parameter. Indeed, the faster the robot reaches the antinode, the quicker the vibration of the cable is reduced. Additionally, we also desire to minimize the steady state error to ensure that the robot reaches and stays at the antinode. With these specified requirements, we can iterate the values of k_p and k_d. Figures 5-(a) and (b) show the horizontal displacement of the mobile robot as a function of time when the robot is subject to step

ASME Letters in Dynamic Systems and Control. Received August 20, 2020;
Accepted manuscript posted April 01, 2021. doi:10.1115/1.4050957

inputs corresponding to the target antinode. For different combinations of k_p and k_d we obtain a different response. Figure 5-(a) shows that without a proportional gain, the robot cannot follow the target and stays at its original location. The results also show that without a derivative gain, the robot moves, but it showcases significant overshoot and steady state error. Furthermore, when k_p matches k_d, the robot moves to the desired location but it still shows significant overshoot. However, over time, the device settles to the target antinode (minimal steady state error).

Figure 5-(b) is a further investigation of the combination of k_p and k_d. It is important to note that for controller gain, in general, it is the relative value between a gain and another that impacts the performance of the controller. The results in Fig. 5-(b) show that when k_p is larger than k_d we get significant overshoot, but there is no significant steady state error. When k_d is larger, we can observe that the percent overshoot significantly decreases, and the steady error also remains small. This finding suggests that with k_d larger than k_p, we can meet the specified performance requirements of the proposed mobile robot for wind-induced vibration control of power lines. For the subsequent work, we will use $k_p = 1$ and $k_d = 6$.

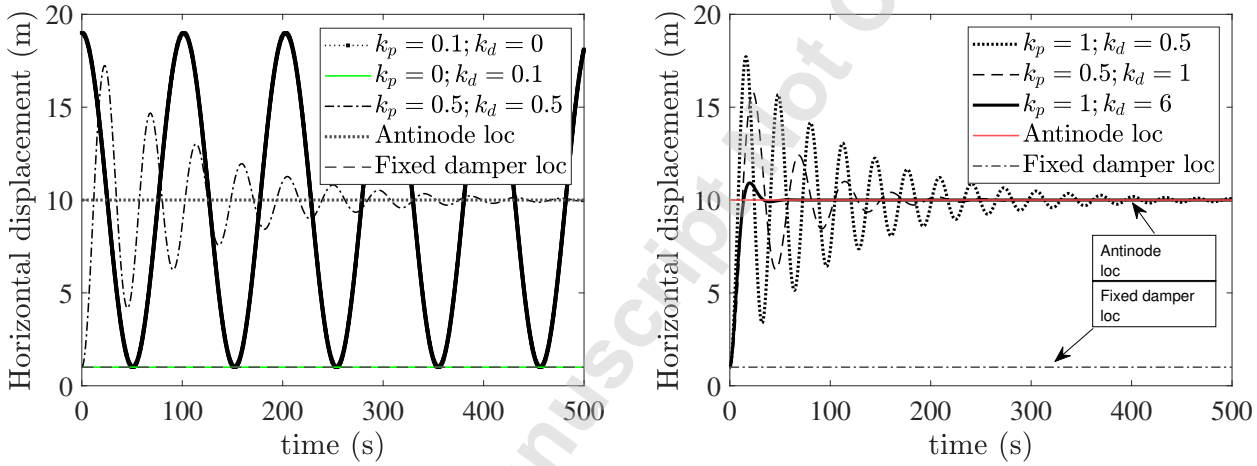

FIGURE 5: COMPARING THE VALUES OF k_p AND k_d FOR OPTIMAL CONTROL

We have shown how to select k_p and k_d , we now focus on the required target location for maximum vibration reduction. The optimal location for vibration suppression corresponds to the conductor's antinodes [27]. For Aeolian vibrations, the wind frequency input ranges from 3 Hz to 150 Hz. Considering this frequency range, a frequency analysis can be done to evaluate the effect of the robot position on the achieved vibration attenuation. Figure 6 shows the frequency responses of the bare cable (Fig. 6-(a)) and the mobile vibration absorber (Fig. 6-(b)) attached to the cable at different positions as the wind excitation frequency varies. The frequency in Figure 6 is normalized by the cable fundamental frequency. The results show that the worst case frequencies corresponds to low harmonics. The vibration of the cable depends on the absorber position. The contour figures present the region of high vibration in yellow and the region of low vibration node in blue. If the absorber is tuned to the wind input frequency and it is properly placed at an antinode, it becomes fully effective by mitigating the vibration of the cable. On the other hand, if the absorber coincides with a node, it becomes ineffective. Consequently, we understand

ASME Letters in Dynamic Systems and Control. Received August 20, 2020;
Accepted manuscript posted April 01, 2021. doi:10.1115/1.4050957

that FVAs will be limited because there is a chance that the FVA position may coincide with a node, especially at higher frequencies (See Fig. 6-(b)). Moreover, the relevance of the mobile damping robot becomes apparent. By consistently self-adjusting its position to an antinode, the mobile damping robot can potentially increase its effectiveness.

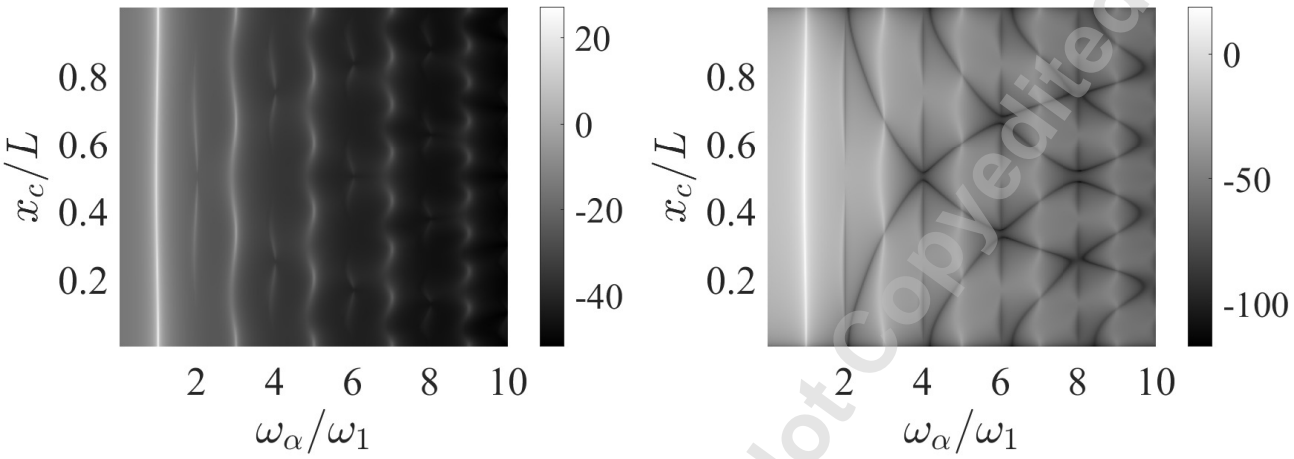

(a) Normalized cable frequency response along the span

(b) Normalized mobile damping robot frequency response along the span

FIGURE 6: FREQUENCY RESPONSE OF THE CABLE AND THE ROBOT ALONG THE SPAN

Having established that the position of the damper is key for vibration reduction, we now compare the performance of a fixed damper to the moving damper. From the literature on vibration design [27], if the damper is well tuned and does not fall on a node, it should provide significant vibration reduction. Additionally, the closer it is to the antinode, the better the vibration reduction should be. In the following, we test this theory by placing the fixed damper and the moving damper at the same initial location and we determine the performance of each device. Figure 7 shows the response of the cable when attached to a fixed damper and moving damper when the cable is subject to a excitation matching its 10^{th} mode (3.27 Hz). The fixed damper and the moving damper are placed at different locations close to the antinode or node, and we evaluate their performance. The results show that when both devices are placed close to the node, the fixed damper is ineffective. In this case, the cable vibrates at resonance. The moving damper is able to readjust itself to the vibrating loop antinode. This results in significant vibration reduction. The results also show that when the dampers are placed within the vibrating loop their performance is comparable. Additionally, the results also show that the vibration mitigation is maximized at the antinode. In summary, we note that as long as the damper is within the vibration loop and is tuned to the resonance frequency, it is effective to reduce vibration. However, if the damper gets close or coincides with a node, it loses its efficiency. In these cases, the proposed moving robot becomes the solution of choice as it can move towards the antinode and maximize vibration reduction.

Having established that the moving damper ensures vibration reduction by being able to avoid nodes, we now focus on a parametric study. In particular, we attempt to evaluate the impact of the relative mass

ASME Letters in Dynamic Systems and Control. Received August 20, 2020;
Accepted manuscript posted April 01, 2021. doi:10.1115/1.4050957

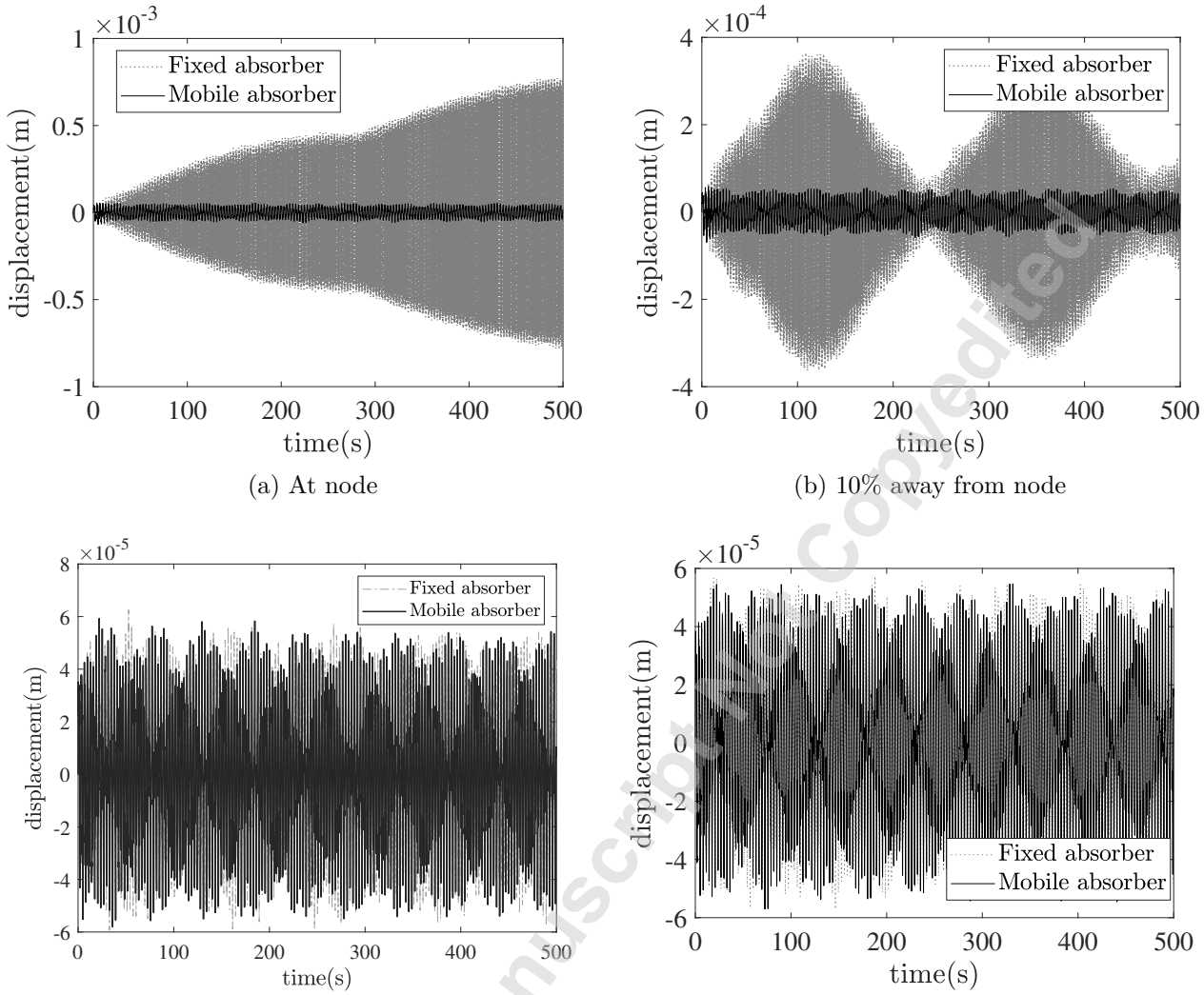

(a) At node

(b) 10% away from node

(c) 30% away from antinode

(d) At antinode

FIGURE 7: COMPARISON OF A FIXED DAMPER AND THE MOBILE DAMPING ROBOT FOR $w_{10} = 3\text{Hz}$

of the in-span mass to the suspended damper mass. For this, we consider the total mass of the device which represents 8% of the total mass of the cable. We then vary the relative mass of the in-span to the suspended mass by introducing the parameter α. α ranges from 10% to 90% of the total mass m_T of the moving device. The in-span mass is then obtained as $m_1 = \alpha m_T$ and the suspended mass is obtained as $m_2 = (1-\alpha)m_T$. Figure 8-(a) shows the displacement of the cable as a function of time for each moving damper assembly. Figure 8-(b) shows the maximum displacement of the cable as a function of α. The results show that increasing the in-span mass degrades the performance of the mobile device. Indeed, as the in-span mass increases, the maximum displacement of the cable increases at steady state. It can also be said that the vibration reduction is maximized for a larger suspended mass relative to the in-span mass. Thus for future design consideration, the in-span mass needs to be minimized.

ASME Letters in Dynamic Systems and Control. Received August 20, 2020;
Accepted manuscript posted April 01, 2021. doi:10.1115/1.4050957

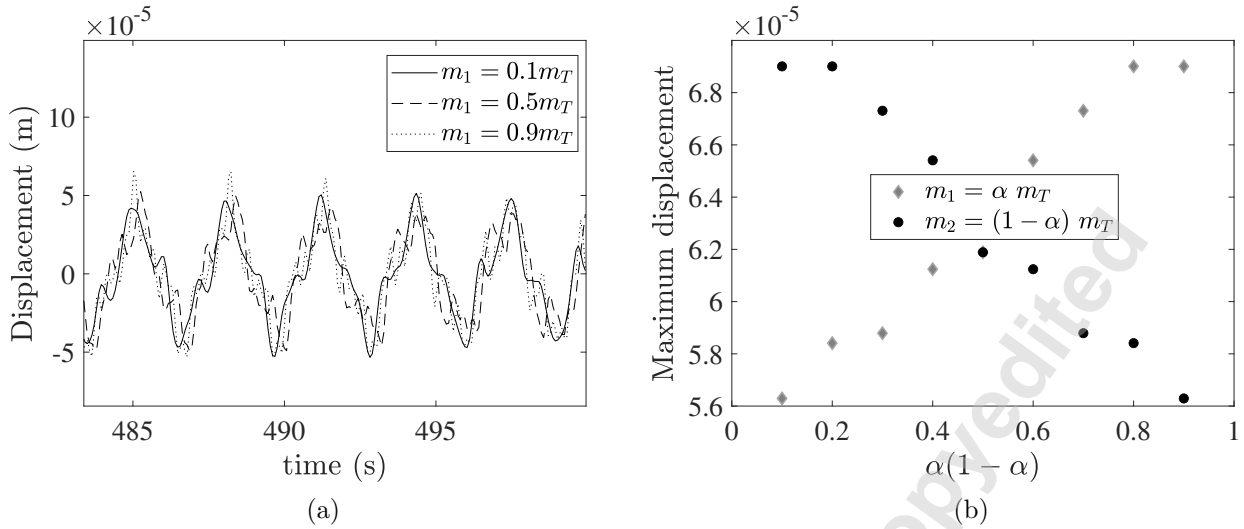

FIGURE 8: COMPARING THE EFFECT OF MASS RATIO OF THE MOBILE ROBOT

CONCLUSION

In this paper, a mobile damping robot was modeled and analyzed to determine its performance in vibration mitigation of power lines. This work contributes to the ongoing research of continuous systems vibration mitigation. The proposed solution tracks the cable antinodes as the wind characteristic changes. The findings showed that when both the fixed damper and moving damper fall within a vibration loop, vibration reduction performance is comparable if both devices are properly tuned. However, the moving damper outperforms the fixed damper when the latter falls close to a node, Moreover, the numerical simulations showed that decreasing the in-span mass relative to the suspended mass maximizes vibration reduction. The current study sets a platform to design a prototype robot to gather data and understand the interaction between the power line and the MDR. For future work, the focus will be given to the control framework that helps the MDR to detect and actively track the antinode. This control framework will be compared to the simple PD controller used in this study. Moreover, more parametric studies could be done to tackle questions that involve the robot power management and overall efficiency.

Acknowledgment

This work is supported in part by by the National Science Foundation (NSF) Grant ECCS-1944032: CAREER: Towards a Self-Powered Autonomous Robot for Intelligent Power Lines Vibration Control and Monitoring.

Conflict of Interest

The authors declare that they have no conflict of interest.

REFERENCES

[1] Vecchiarelli, J., Currie, I., and Havard, D., 2000. "Computational analysis of aeolian conductor vibration with a stockbridge-type damper". *Journal of Fluids and Structures,* ***14***(4), pp. 489–509.

[2] Lu, M., and Chan, J., 2007. "An efficient algorithm for aeolian vibration of single conductor with multiple dampers". *IEEE Transactions on power Delivery,* ***22***(3), pp. 1822–1829.

[3] Barry, O., Oguamanam, D. C., and Lin, D. C., 2013. "Aeolian vibration of a single conductor with a stockbridge damper". *Proceedings of the Institution of Mechanical Engineers, Part C: Journal of Mechanical Engineering Science,* ***227***(5), pp. 935–945.

[4] Barry, R. O., 2014. "Vibration modeling and analysis of a single conductor with stockbridge dampers". PhD thesis.

[5] Barry, O., Zu, J., and Oguamanam, D., 2015. "Analytical and experimental investigation of overhead transmission line vibration". *Journal of Vibration and Control,* ***21***(14), pp. 2825–2837.

[6] Barry, O., Zu, J., and Oguamanam, D., 2015. "Nonlinear dynamics of stockbridge dampers". *Journal of Dynamic Systems, Measurement, and Control,* ***137***(6), p. 061017.

[7] Barry, O., Long, R., and Oguamanam, D., 2017. "Simplified vibration model and analysis of a single-conductor transmission line with dampers". *Proceedings of the Institution of Mechanical Engineers, Part C: Journal of Mechanical Engineering Science,* ***231***(22), pp. 4150–4162.

[8] of Economic Advisers, P. C., 2013. "Economic benefits of increasing electric grid resilience to weather outages.". pp. 163–178.

[9] Katrasnik, J., Pernus, F., and Likar, B., 2009. "A survey of mobile robots for distribution power line inspection". *IEEE Transactions on power delivery,* ***25***(1), pp. 485–493.

[10] Miller, R., Abbasi, F., and Mohammadpour, J., 2017. "Power line robotic device for overhead line inspection and maintenance". *Industrial Robot: An International Journal*.

[11] Lima, E. J., Bomfim, M. H. S., and de Miranda Mourão, M. A., 2018. "Polibot–power lines inspection robot". *Industrial Robot: An International Journal*.

[12] EPRI, U., and R&D, E., 2006. Profiling and mapping of intelligent grid r&d programs. Tech. rep., Palo Alto, CA: US EPRI.

[13] Myung, H., Wang, Y., Kang, S., and Chen, X., 2014. "Survey on robotics and automation technologies for civil infrastructure".

[14] Phillips, A., Engdahl, E., McGuire, D., Major, M., and Bartlett, G., 2012. "Autonomous overhead transmission line inspection robot (ti) development and demonstration". In 2012 2nd International Conference on Applied Robotics for the Power Industry (CARPI), IEEE, pp. 94–95.

[15] Cho, K. H., Jin, Y. H., Kim, H. M., Moon, H., Koo, J. C., and Choi, H. R., 2016. "Multifunctional robotic crawler for inspection of suspension bridge hanger cables: Mechanism design and performance validation". *IEEE/ASME Transactions on Mechatronics,* ***22***(1), pp. 236–246.

[16] Almadhoun, R., Taha, T., Seneviratne, L., Dias, J., and Cai, G., 2016. "A survey on inspecting structures using robotic systems". *International Journal of Advanced Robotic Systems,* ***13***(6), p. 1729881416663664.

[17] Yang, L., Fu, C., Li, Y., and Su, L., 2019. "Survey and study on intelligent monitoring and health management for large civil structure". *International Journal of Intelligent Robotics and Applications,* ***3***(3), pp. 239–254.

[18] Pouliot, N., Richard, P.-L., and Montambault, S., 2015. "Linescout technology opens the way to robotic inspection and maintenance of high-voltage power lines". *IEEE Power and Energy Technology*

Systems Journal, ***2***(1), pp. 1–11.
[19] Fei, J., Lin, B., Yan, S., Ding, M., Xiao, J., Zhang, J., Zhang, X., Ji, C., and Sui, T., 2017. "Chatter mitigation using moving damper". *Journal of Sound and Vibration,* ***410***, pp. 49–63.
[20] Wang, Y., and Lo, C., 2014. "Design of hybrid dynamic balancer and vibration absorber". *Shock and Vibration,* ***2014***.
[21] Barry, O., and Bukhari, M., 2017. "On the modeling and analysis of an energy harvester moving vibration absorber for power lines". In ASME 2017 Dynamic Systems and Control Conference, American Society of Mechanical Engineers Digital Collection.
[22] Bukhari, M. A., Barry, O., and Tanbour, E., 2018. "On the vibration analysis of power lines with moving dampers". *Journal of vibration and control,* ***24***(18), pp. 4096–4109.
[23] Paul, K.and Oumar, B., 2020. "On the vibration suppression of power lines using mobile damping robots". *Engineering Structures, submitted*.
[24] Barry, O. R., Tanbour, E. Y., Vaja, N. K., and Tanbour, H., 2018. Asymmetric aeolian vibration damper, Apr. 17. US Patent 9,948,081.
[25] Foti, F., and Martinelli, L., 2016. "Mechanical modeling of metallic strands subjected to tension, torsion and bending". *International Journal of Solids and Structures,* ***91***, pp. 1–17.
[26] Meirovitch, L., 2010. *Fundamentals of vibrations*. Waveland Press.
[27] Inman, D. J., and Singh, R. C., 1994. *Engineering vibration*, Vol. 3. Prentice Hall Englewood Cliffs, NJ.

